J Sol-Gel Sci Technol (2012) 61:390–402
DOI 10.1007/s10971-011-2639-9

ORIGINAL PAPER

Photocatalytic degradation of metoprolol in water suspension of TiO_2 nanopowders prepared using sol–gel route

Maja Šćepanović · Biljana Abramović · Aleksandar Golubović · Sanja Kler · Mirjana Grujić-Brojčin · Zorana Dohčević-Mitrović · Biljana Babić · Branko Matović · Zoran V. Popović

Received: 8 September 2011 / Accepted: 21 November 2011 / Published online: 30 November 2011

Abstract Nanocrystalline titanium dioxide (TiO_2) powders have been synthesized by sol–gel method using titanium tetrachloride ($TiCl_4$) or tetrabutyl titanate ($Ti(OC_4H_9)_4$ as precursors, different alcohols and calcination temperatures in the range from 400 to 650 °C. The photocatalytic activity of as-prepared powders has been tested for the degradation of metoprolol tartrate salt, a selective β-blocker used to treat a variety of cardiovascular diseases, and compared to photocatalytic activity obtained from Degussa P25. Nanosized TiO_2 powders prepared from $TiCl_4$ and amyl-alcohol, calcined at 550 °C, displayed an activity comparable to Degussa P25, whereas the sample from the same series, calcined at 650 °C, showed higher photocatalytic activity in the whole range of the catalyst loading. Structural, morphological and surface properties of synthesized TiO_2 nanopowders have been investigated by XRD, SEM, EDS and BET measurements, as well as FTIR and Raman spectroscopy, in order to find out the material properties which enable rapid an efficient decomposition of metoprolol under UV radiation.

M. Šćepanović (✉) · A. Golubović · M. Grujić-Brojčin · Z. Dohčević-Mitrović · Z. V. Popović
Institute of Physics, University of Belgrade, Pregrevica 118, 11080 Belgrade, Serbia
e-mail: maja@ipb.ac.rs

B. Abramović · S. Kler
Department of Chemistry, Biochemistry and Environmental Protection, Faculty of Sciences, University of Novi Sad, Trg D. Obradovića 3, 21000 Novi Sad, Serbia

B. Babić · B. Matović
Institute of Nuclear Sciences "Vinča", University of Belgrade, 11001 Belgrade, Serbia

Keywords Nanopowder · TiO_2 · Sol–gel synthesis · Raman spectroscopy · Photocatalysis

1 Introduction

Pharmaceuticals, as a large group of human and veterinary medicinal compounds, are considered as an emerging environmental problem, due to long term usage worldwide. Its continuous input and persistence to the aqueous system, even at low concentrations, may result in a potential risk for aquatic and terrestrial organisms. Cardiovascular drugs are among most frequently detected pharmaceuticals in wastewaters, where, according to literature, β-blocker metoprolol is listed in concentration of 10–390 ng L^{-1} [1]. Although in trace concentrations, those pharmaceuticals are persistent against biological degradation and they retain their chemical structure long enough and their presence in the environment is considered potentially dangerous.

Metoprolol tartrate salt (1-[4-(2 methoxyethyl)phenoxy]-3-(propan-2-ylamino)propan-2-ol tartrate (2 : 1), CAS No 56392-17-7, $(C_{15}H_{25}NO_3)_2$ $C_4H_6O_6$, M_r = 684.81, MET) is a selective β-blocker that is used to treat a variety of cardiovascular diseases, such as hypertension, coronary artery disease, and arrhythmias, by blocking the action of epinephrine and norepinephrine on the β-adrenergic receptors in the body, primarily in the heart [2]. Wide use of MET in recent years has a consequence in increasing concentrations of this pharmaceutical in aqueous effluents [3, 4]. MET shows slow direct phototransformation and/or hydrolysis [5, 6]. An efficient way to deal with this problem is degradation of the drug by advanced oxidation processes (AOPs) based on the formation of hydroxyl ($^{\bullet}OH$) and other radicals that oxidize

toxic and non-biodegradable compounds to the different co-products, and, in the course of time, to inert final products [7]. MET contains a secondary amine group and a weakly/moderately activated aromatic ring that are probable targets of molecular ozone and attacks of $^{\bullet}OH$ [2]. Yang et al. [8] investigated degradation of selected β-blockers (atenolol, metoprolol, and propranolol) in aqueous suspensions of TiO_2 Degussa P25 and proposed a preliminary mechanism of degradation of these compounds. Romero et al. [9, 10] have also investigated and compared degradation intermediates of metoprolol and propranolol by AOPs.

Titanium dioxide (TiO_2) is recognized as catalyst employed for almost all the pharmaceuticals photocatalytic treatment studies, as inexpensive, commercially available at various crystalline forms and particle characteristics, non-toxic and photochemically stable material [11]. Degussa P25, a commercially available powder is a mixture of anatase and rutile phases (with 80% of anatase approximately [12]), showing exceptional photocatalytic performance, superior to other grades of TiO_2 [13].

We synthesized TiO_2 nanopowders via sol–gel routine to obtain photocatalyst efficient in metoprolol degradation. The sol–gel is solution-based technique, where material structure is created through chemical reactions in liquid state. It has recently received more attention in production of high performance nanostructured materials, where morphology, surface area, average nanocrystallite size, crystallinity, and phase structure are controlled by sol–gel synthesis parameters [14]. The properties of sol–gel synthesized TiO_2 nanopowders are determined by the key sol–gel processing parameters such as the precursor type, pH value in hydrolysis process, duration and temperature of hydrolysis (aging), type of alcogel, duration and temperature of drying, and calcination conditions (heating rate, temperature, duration and cooling rate) [15].

In this paper we investigate the influence of sol–gel synthesis condition on photocatalytic properties of TiO_2 nanopowders, by varying some synthesis parameters (precursor, alcohol, basic solution, and calcination temperature) aiming to obtain photocatalyst for degradation of metoprolol, efficient enough in comparison to Degussa P25. Several methods of characterization, such as the X-ray diffraction (XRD), scanning electron microscopy (SEM), energy dispersive X-ray spectroscopy (EDS), Brunauer-Emmett-Teller (BET) measurements, Fourier transform infrared (FTIR) and Raman spectroscopy, are employed to correlate structural and morphological properties of synthesized TiO_2 nanopowders and their photocatalytic activity under ultraviolet (UV) irradiation.

2 Experimental

2.1 Powder synthesis

The TiO_2 nanopowders used as catalysts in this study are synthesized by the sol–gel method, which typically involves hydrolysis of a solution of a precursor molecule in order to obtain a suspension of colloidal particles—gel (at first in the form of hydrogel and then in the form of alcogel). Titanium tetrachloride ($TiCl_4$) and tetrabutyl titanate ($Ti(OC_4H_9)_4$) are the precursors commonly used in sol–gel synthesis, which required different procedures in alcogel production:

(1) In synthesis with *tetrabutyl titanate* as precursor, ethanol (EtOH) is used as the solvent, hydrochloride acid as the catalyst, and water for hydrolysis. The hydrolysis and polycondensation reactions of $Ti(OC_4H_9)_4$ were carried out at the room temperature, whereas the measured pH value of solution was 7.0. The reagent molar ratio was $Ti(OC_4H_9)_4$:EtOH:HCl:H_2O = 1:15:0.3:4 [16]. After the gelation, the wet gels were dried at 80 °C;

(2) In synthesis with *titanium tetrachloride* as the precursor, $Ti(OH)_4$ hydrogel was obtained by hydrolysis of $TiCl_4$ at 0 °C with controlled addition of 2.5 wt% alkalic solution (NH_4OH or NaOH) into the aqueous solution of $TiCl_4$ (0.3 M) and careful control of the pH value (9.3) of the solution [15]. After aging (fixed time of 5 h) [17], as-prepared hydrogel was filtered and rinsed out with distilled water until complete removal of chloride ions. The absence of Cl^- ions was checked using 0.1 M solution of $AgNO_3$. Obtained $Ti(OH)_4$ hydrogel was converted to its alcogel by repeated exchange with corresponding alcohol for several times. Also, different alcohols were used to investigate the influence of the type of alcogel on properties of photocatalysis: *methanol, ethanol, 2-propanol, amylalcohol* and *glycerol*. The alcogels were dried at 280 °C during 4 h.

The TiO_2 nanopowders produced by one of the procedures described above are amorphous. During the calcination process at temperature of 350 °C or higher, the crystalline anatase phase is formed [18]. As calcination temperature approaches ~600 °C, the phase transition from anatase to rutile starts [19]. However, high calcination temperature results in the growth of nanocrystalline particles and the rapid decrease of specific surface area. To investigate the influence of temperature of calcination, few samples synthesized with the same alcohol (amylalcohol) were exposed to different calcination temperatures (400, 550 and 650 °C). The duration of calcination process (7 h) and temperature gradient of the heating (135 °C h^{-1}) were the same in all the experiments.

The scheme of the TiO_2 production by sol–gel process can be written as follows:

$$TiCl_4 \text{ or } Ti(OC_4H_9)_4 \rightarrow Ti(OH)_4 \rightarrow \text{alcogel} \xrightarrow{\text{calcination}} TiO_2 \quad (1)$$

The samples synthesized by described procedures are listed in Table 1, together with variable parameters of synthesis (precursor, alcohol, basic solution, and calcination temperature).

All chemicals in this experiment were analytical grades, used as received. Tetrabutyl titanate 99% was produced by Acros Organics, $TiCl_4$ and glycerol by Merck Chemicals, amylalcohol by Lacheme, ethanol by J. T. Backer, methanol and 2-propanol by Centrohem, 25% NH_4OH by Carbo Erba and NaOH by MP Hemija.

2.2 Characterization methods

Powder XRD patterns of TiO_2 nanopowders were recorded by Siemens X-ray Diffractometer (Kristaloflex 500) with Ni filtered CuKα radiation and using Si as an external standard. The measurements were performed in the 2θ range from 20° to 80° in a continuous scan mode with a step width of 0.02° and at a scan rate of 1° 2θ min^{-1}.

Morphology of the catalyst is determined by SEM. Gold coated particles were observed on SEM type JEOL JSM-6460LV with the operating voltage of 20 keV. Composition/quality of TiO_2 was analyzed on SEM with EDS detector. EDS are performed by INCAx-sight detector and "INAx-stream" pulse processor (Oxford Instruments).

The powder specific surface area of the samples was calculated following the multipoint BET procedure on Quantachrome ChemBet-3000 setup. The particle size distribution (PSD) was derived from nitrogen adsorption/desorption isotherms obtained at 77 K.

The IR reflection spectra of TiO_2 nanopowders pressed into pellets were measured at room temperature using a BOMEM-DA8 spectrometer in the spectral range between 400 and 4,000 cm^{-1}.

Raman scattering measurements of TiO_2 samples was performed in the backscattering geometry at room temperature in the air using Jobin–Yvon T64000 triple spectrometer, equipped with a confocal microscope and a nitrogen-cooled charge coupled device detector. The spectra excited by 514.5 nm line of Ar^+/Kr^+ ion laser with output power less than 5 mW to avoid local heating due to laser irradiation.

2.3 Photocatalytic activity

The photocatalytic activity of the TiO_2 nanopowders was evaluated by the degradation of the solution of metoprolol tartrate salt (≥99%, Sigma–Aldrich). Photocatalytic degradation was carried out in a cell made of Pyrex glass (total volume of ca. 40 mL, liquid layer thickness 35 mm), with a plain window on which the light beam was focused. The cell was equipped with a magnetic stirring bar and a water circulating jacket. A 125 W high-pressure mercury lamp (Philips, HPL-N, emission bands in the UV region at 304, 314, 335 and 366 nm, with maximum emission at 366 nm), together with an appropriate concave mirror, was used as the radiation source. The output for the mercury lamp was calculated to be ca. 8.8×10^{-9} Einstein mL^{-1} min^{-1} (potassium ferrioxalate actinometry).

In a typical experiment the initial MET concentration was 0.05 mM and the TiO_2 loading was 1.0 mg mL^{-1}, unless otherwise is stated. The total suspension volume was 20 mL. The aqueous suspension of TiO_2 was sonicated (50 Hz) in the dark for 15 min before illumination, to uniformly disperse the photocatalyst particles and attain adsorption equilibrium. The suspension thus obtained was thermostated at 25 ± 0.5 °C in a stream of O_2 (3.0 mL min^{-1}), and then irradiated. During irradiation,

Table 1 The list of sol–gel synthesis parameters

Sample name	Precursor	Alcohol	Basic solution	Calcination temperature (°C)
$T(BE)_{550}$	Tetrabutyl titanate (B)	Ethanol (E)	–	550
$T(CEA)_{550}$	Titanium tetrachloride (C)	Ethanol (E)	NH_4OH (A)	550
$T(CPA)_{550}$	Titanium tetrachloride (C)	2-Propanol (P)	NH_4OH (A)	550
$T(CAA)_{550}$	Titanium tetrachloride (C)	Amylalcohol (A)	NH_4OH (A)	550
$T(CMA)_{550}$	Titanium tetrachloride (C)	Methanol (M)	NH_4OH (A)	550
$T(CGA)_{550}$	Titanium tetrachloride (C)	Glycerol (G)	NH_4OH (A)	550
$T(CAN)_{400}$	Titanium tetrachloride (C)	Amylalcohol (A)	NaOH (N)	400
$T(CAN)_{550}$	Titanium tetrachloride (C)	Amylalcohol (A)	NaOH (N)	550
$T(CAN)_{650}$	Titanium tetrachloride (C)	Amylalcohol (A)	NaOH (N)	650

The sample name is generated as follows: the first letter in brackets corresponds to precursor, 2nd to alcohol, and 3rd one to basic solution, which are abbreviated as shown in the Table. The subscript denotes calcination temperature

the mixture was stirred at a constant rate under continuous O_2 flow. Control experiments were carried out under O_2 flow but by stopping the irradiation showed that there were no losses of volatile compounds during the degradation. All experiments were performed at the natural pH.

For the LC–DAD kinetic studies of MET photodegradation, aliquots of 0.50 mL were taken from the reaction mixture at the beginning of the experiment and at regular time intervals. Aliquot sampling caused a maximum volume variation of ca. 10% in the reaction mixture. The suspensions containing photocatalyst were filtered through Millipore (Milex-GV, 0.22 μm) membrane filter. Lack of adsorption of MET on the filters was preliminary checked. After that, a 20-μL sample was injected and analyzed on an Agilent Technologies 1100 Series liquid chromatograph, equipped with an Eclypse XDB-C18 column (150 mm × 4.6 mm i.d., particle size 5 μm, 25 °C). The UV/vis DAD detector was set at 225 nm (wavelength of MET maximum absorption). The mobile phase (flow rate 0.8 mL min^{-1}) was a mixture of acetonitrile (ACN, 99.8%, J. T. Baker) and water (with the following gradient: 0 min 15% ACN, 5 min 30% ACN and 5 min 30% ACN; post time 3 min), the water being acidified with 0.1% H_3PO_4 (85%, Lachema, Neratovice).

Commercially available TiO_2, Degussa P25 (75% anatase and 25% rutile, specific area of 50 m^2 g^{-1}, and average particle size about 20 nm, according to the producer's specification), was used for the purpose of comparison.

3 Results

3.1 XRD

The XRD patterns of chosen TiO_2 nanopowders are presented in Fig. 1. The diffraction peaks present in all samples coincide to anatase TiO_2 structure (JCPDS card 21-1272, space group $I4_1/amd$). Their positions are slightly shifted, indicating a change in lattice parameters in comparison to the bulk values for anatase ($a_0 = 0.37852$ nm, $c_0 = 0.95139$ nm), as shown in Table 2. Consequently, the lattice volume of anatase in all synthesized nanopowders is smaller than in its bulk counterpart ($V_0 = 136.3127 \times 10^{-3}$ nm). It has been noticed that positive pressure caused by large surface hydration could be a primary reason for lattice contraction volume in anatase nanostructures [20, 21].

The average crystallite size of the anatase nanoparticles, estimated by using Scherrer's equation, is in range from 13 to 17 nm, as listed in Table 2. A whole powder pattern structure refinement using the structure analysis software Power Cell [22] was also carried out. As expected, structural analysis gives slightly higher values for crystallite size in comparison to Scherrer method, because the effects of microstrain are taken into account.

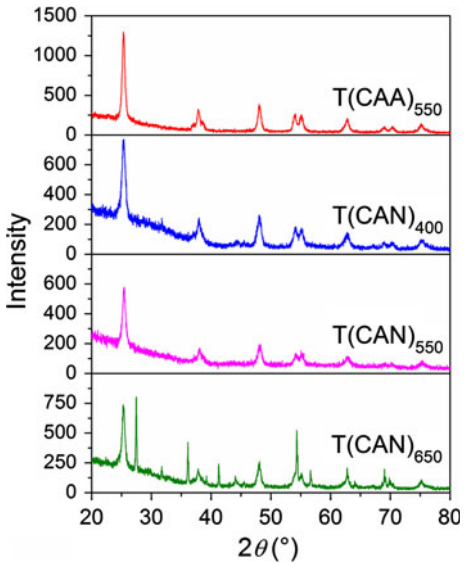

Fig. 1 The XRD diffractograms of some synthesized TiO_2 nanopowders

Note that diffraction peaks of brookite phase are not seen in XRD patterns of TiO_2 nanopowders, whereas the peaks corresponding to the rutile phase (JCPDS card no. 21-1276, space group $P4_2/mnm$) are observed in the diffractogram of sample $T(CAN)_{650}$. The amount of rutile phase in this sample is estimated to be ~30% according to Power Cell. The lack of the reliable results for crystallite size and microstrain in $T(CAN)_{650}$ is probably related to the presence of rutile phase in this sample.

3.2 SEM/EDS

The SEM images of two synthesized TiO_2 nanopowders ($T(CAA)_{550}$, $T(CAN)_{650}$) and Degussa P25 are presented in Fig. 2. As can be seen from the micrographs, most of the particles in this sample have a spherical shape, with a grain diameter, roughly estimated to be about 23 nm in synthesized samples, and around 29 nm in Degussa P25. Table 3 presents the chemical composition of the same nanopowders, estimated by EDS spectra (Fig. 3, upper row), which correspond to framed area of micrographs (Fig. 3, lower row). In the samples analyzed here, oxygen weight percent is higher than in stoichiometric TiO_2 (40 wt%), with the exception of the sample $T(CAN)_{550}$. Among synthesized samples, the highest value of oxygen weight percent (but still lower than value in Degussa P25) is registered in $T(CAN)_{650}$. The EDS analysis has also shown the presence of sodium (Na) and very low concentration (<1 wt%) of chlorine (Cl) in the samples synthesized from NaOH as basic solution and $TiCl_4$ as precursor (Table 3). Note here also that hydrogen cannot be detected by EDS method.

Table 2 Lattice parameters, crystallite size L (obtained from Scherrer method and structure analysis by Power Cell), and microstrain ε (also from Power Cell) for anatase phase in some TiO_2 nanopowders

Sample	Lattice parameters (nm)		Lattice volume	Scherrer method	Structure analysis (Power Cell)	
	$a(= b)$	c	V (10^{-3} nm)	L (nm)	L (nm)	ε (%)
$T(CAA)_{550}$	0.37822	0.94938	135.8092	17	22	0.19
$T(CAN)_{400}$	0.37859	0.94780	135.8485	14	21	0.26
$T(CAN)_{550}$	0.37852	0.94841	135.8857	13	17.5	0.20
$T(CAN)_{650}$	0.37832	0.94887	135.8080	14	–	–

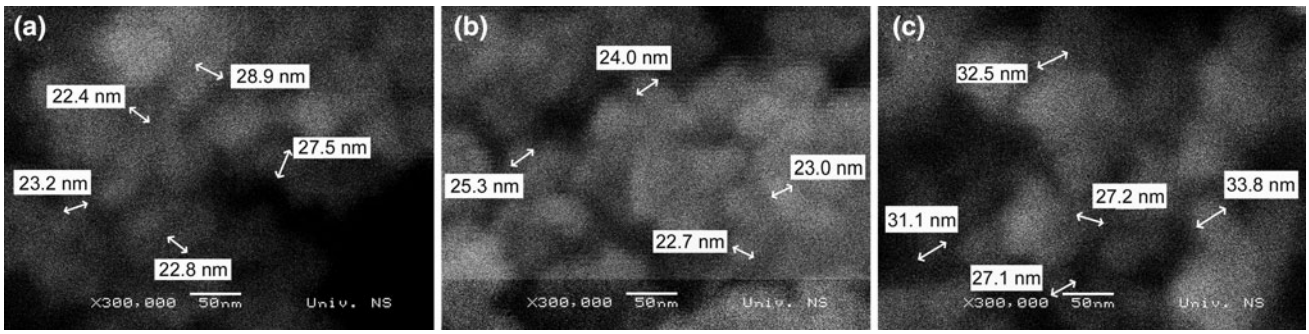

Fig. 2 SEM micrographs of TiO_2 nanopowders $T(CAA)_{550}$ (**a**) and $T(CAN)_{650}$, (**b**), compared to Degussa P25 (**c**)

Table 3 EDS results for some TiO_2 nanopowder samples and Degussa P25

Sample	O (wt%)	Ti (wt%)	Na (wt%)	Cl (wt%)	Total (wt%)
$T(CAA)_{550}$	42.60	57.40	–	–	100.00
$T(CAN)_{400}$	47.81	47.29	4.44	0.46	100.00
$T(CAN)_{550}$	32.72	64.54	1.84	0.90	100.00
$T(CAN)_{650}$	50.46	46.63	2.24	0.67	100.00
Degussa P25	57.52	42.48	–	–	100.00

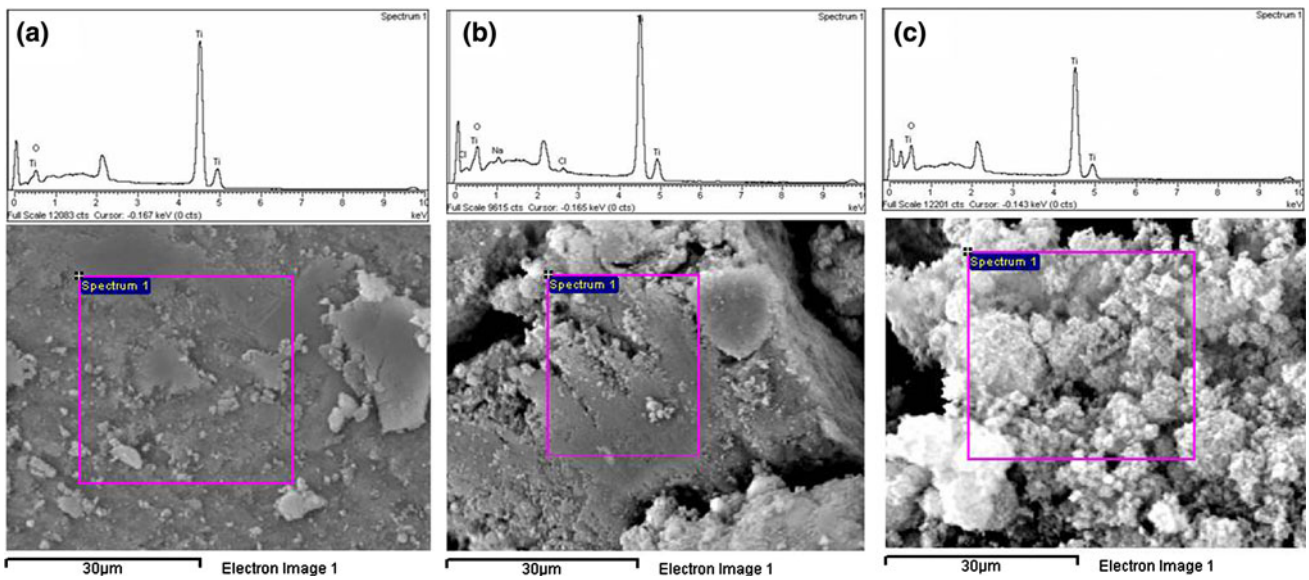

Fig. 3 SEM images with corresponding EDS spectra of TiO_2 nanopowders $T(CAA)_{550}$ (**a**), $T(CAN)_{650}$ (**b**) and Degussa P25 (**c**)

3.3 BET

The values of the BET specific surface areas (S_{BET}) of some TiO_2 nanopowders are given in the Table 4, together with pore volume (V_p) and pore diameter (D_p). The sample $T(CAN)_{400}$ exhibits the lowest specific surface area (32 m^2 g^{-1}), whereas S_{BET} ranges between 51 and 63 m^2 g^{-1} in the rest of the samples. All nanopowders listed here, as well Degussa P25, are mostly mesoporous (pore diameters of 2–50 nm, $S_{BET} \approx S_{meso}$). However, mean pore diameter of synthesized samples, which is in the range of 6–7 nm, is much lower than the corresponding one of Degussa P25 (31.5 nm [12]).

The PSD of specified synthesized samples are bimodal (Fig. 4), with the first mode peaked in the range 2–3 nm, and the second mode around 4 nm. Among these samples, the $T(CAN)_{650}$ contains the greatest number of pores with diameter higher than 3 nm, whereas the number of such pores in $T(CAN)_{400}$ is the smallest.

3.4 FTIR

The IR reflectivity spectra of representative TiO_2 nanopowders in the range of 450–4,000 cm^{-1} are presented in Fig. 5. The spectra are dominated by the features in the range of 450–1,000 cm^{-1}, which can be related to the surface vibration of Ti–O bonds [23, 24]. It is obvious that more features in this region appear in the samples with mixed anatase/rutile phase ($T(CAN)_{650}$ and Degussa P25), as rutile has one more IR active mode than anatase in specified region [25]. Also, nanostructure of analyzed powders has strong influence on the shape of IR reflectivity spectra [26], but this is beyond the scope of this study.

The reflectivity spectra of the same samples in the region of 1,200–4,000 cm^{-1} are shown enlarged in the Inset of the Fig. 5. The main spectral features in this region appear around 1,260 cm^{-1}, between 1,400 and 1,800 cm^{-1}, and in the ranges of 2,800–3,000 cm^{-1} and 3,200–3,800 cm^{-1}. The band at about 1,260 cm^{-1}, which is most prominent in the IR spectrum of Degussa P25, was assigned to carbonate [27] or nitrate [28] species at TiO_2 surface. Small bands in the range of 1,400–1,800 cm^{-1} most probably originate from carbonates or hydrogen carbonates groups in TiO_2 [29]. The bands in the range of 2,800–3,000 cm^{-1} can be assigned to the symmetric and asymmetric stretching mode of the C–H bond [30], originating from residues which remain in TiO_2 samples even after calcination.

As TiO_2 surface O–H group nature and distribution are in many cases determining factor of catalyst behaviour, a considerable research has been devoted here to characterizing these groups present at the surface of TiO_2. According to many FTIR studies published in the literature, the vibration band between 3,000 and 3,150 cm^{-1} is

Table 4 Porous properties of TiO_2 samples: specific surface area (S_{BET}), pore volume (V_p) and pore diameter (D_p)

Sample	S_{BET} (m^2/g)	V_p (cm^3/g)	D_p (nm)
$T(CAA)_{550}$	63	0.103	6.5
$T(CAN)_{400}$	32	0.056	6.6
$T(CAN)_{550}$	51	0.092	7.2
$T(CAN)_{650}$	63	0.101	6.4
Degussa P25	51	0.150	31.5

The data for Degussa P25 are taken from the literature, ref. [12]

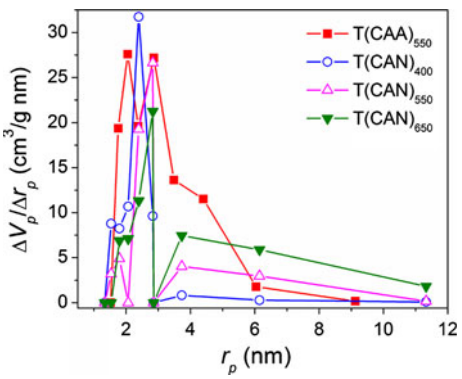

Fig. 4 The pore size distribution of some synthesized TiO_2 nanopowders

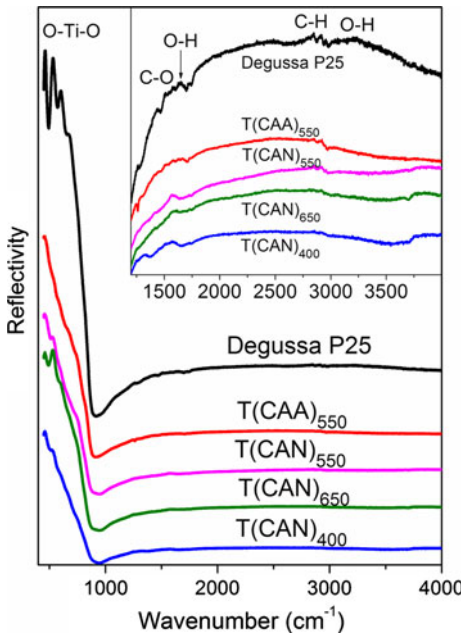

Fig. 5 The IR reflectivity spectra of representative TiO_2 nanopowders. The *inset*: enlarged part of the IR spectra in the region from 1,200 to 4,000 cm^{-1}

associated with the O–H stretching mode of water molecules [31], while that at about 1,630 cm^{-1} is assigned to O–H bending modes [23 and references therein]. The bands in frequency range of 3,150–3,500 cm^{-1} are usually attributed to H-bounded O–H groups, and those in the 3,400–3,600 cm^{-1} region to mixed O–H groups [31]. The bands in the 3,600–3,800 cm^{-1} region are due to stretching modes of different types of free hydroxyl groups adsorbed on the crystalline surfaces of titania or on defects located at the surfaces [23 and references therein]. It should be noted that IR reflectivity spectra of TiO_2 nanopowders, shown in Fig. 5, enable identification of specified surface groups, but do not allow determination of the relation between the amounts of different kinds of these groups at the surface of TiO_2 nanoparticles.

3.5 Raman scattering

The Raman spectra of the samples synthesized by sol–gel method, listed in Table 1, were the subjects of analysis, which indicated anatase as a dominant phase in all samples. The spectrum of the sample $T(CAA)_{550}$ shown in Fig. 6a illustrates characteristic anatase Raman modes in the region of 50–1,000 cm^{-1} and so called C–H and O–H spectral region in the 1,000–4,000 cm^{-1} frequency range.

Generally, the intensity and linewidth of Raman modes provide the information about crystalline quality of the material. According to this, among synthesized samples, $T(CAN)_{650}$ and $T(BE)_{550}$, with the most intensive and narrowest characteristic anatase modes in Raman spectra, have the crystalline quality close to Degussa P25.

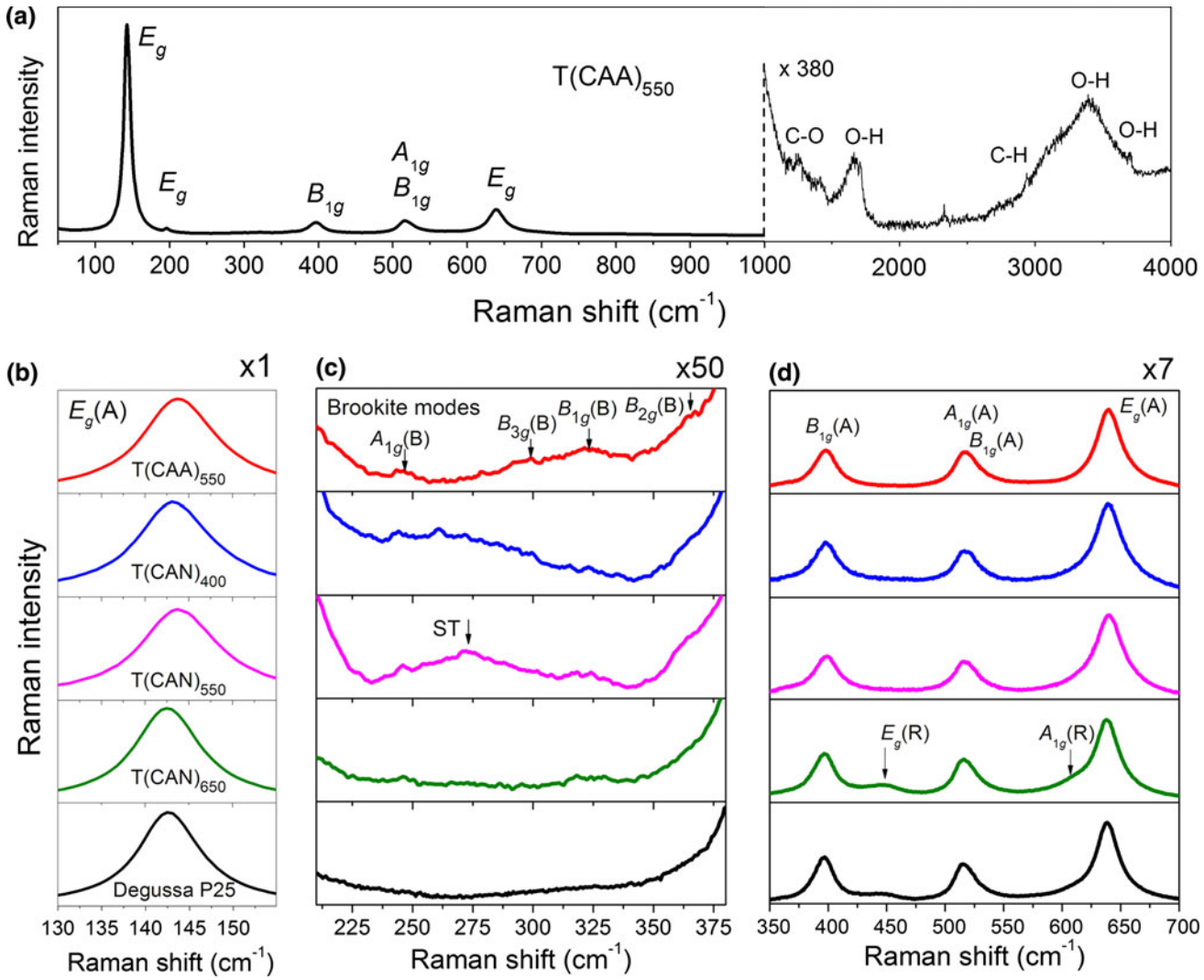

Fig. 6 **a** Raman spectrum of $T(CAA)_{550}$ nanopowder. Spectra of TiO_2 nanopowders divided in three characteristic regions: **b** around anatase E_g mode, **c** 210–380 cm^{-1} (brookite modes), and **d** 350–700 cm^{-1} (anatase, rutile and sodium titanate modes). The intensities of the spectra are normalized to 1 in the first region (E_g) and multiplied by 50 and 7 in following two regions to pronounce corresponding features of the spectra. Anatase, rutile, brookite and sodium titanate are labelled as A, R, B, and ST, respectively

In order to point out some features related to different TiO_2 phases (anatase, brookite and rutile) and the presence of residuals due to synthesis process, Raman spectra of some nanopowders ($T(CAA)_{550}$, $T(CAN)_{400}$, $T(CAN)_{550}$, and $T(CAN)_{650}$), together with Degussa P25, are shown in Fig. 6b–6d. The spectra are divided in three characteristic regions because of different intensities in each of them.

The first region, around anatase E_g Raman mode ($\sim$143 cm^{-1}), is shown in Fig. 6b. The relationship between Raman shift and full width at half maximum (FWHM) of this mode, for all TiO_2 nanopowders, is presented in Fig. 7. These results show that the Raman shift and FWHM of sol–gel synthesized samples are greater than in Degussa P25 nanopowder: Raman shift is positioned between 142.6 cm^{-1} in $T(CAN)_{650}$ and 144.1 cm^{-1} in $T(CGA)_{550}$, whereas the variation of FWHM ranges from 9.4 cm^{-1} in $T(BE)_{550}$ to 12.6 cm^{-1} in $T(CPA)_{550}$. Beside the crystalline quality, Raman shift and linewidth of E_g mode in anatase nanocrystals at given temperature also depend on confinement effects, due to the nanocrystalline size, microstrain and nonstoichiometry [32, 33]. In order to estimate which of those effects has the greatest influence on blueshift and broadening of Raman E_g mode of synthesized nanopowders in comparison to corresponding values in bulk anatase (141 cm^{-1} and 8 cm^{-1} [34]), the relationship between Raman shift and FWHM is calculated by phonon confinement model (PCM) (Fig. 7). The particle size used in the calculation belongs to the range of 17–25 nm, corresponding to the size of nanocrystallites in synthesized powders, estimated from XRD (Table 2). However, for the specified crystallite sizes, the values of Raman shift and FWHM calculated by PCM are lower than experimental ones, even when PCM with inhomogeneous strain is applied (open circles in Fig. 7) [35, 36]. Although widening of E_g mode can be the consequence of lower crystalline quality, it is obvious that, in addition to phonon confinement and microstrain, the nonstoichiometry must be included in the explanation of blueshift and broadening of Raman E_g mode in most of our samples. Namely, it is well known that this mode is blueshifted and broadened due to nonstoichiometry in anatase nanopowders [37].

In order to investigate the presence of brookite phase by Raman spectroscopy, the second region of the Raman spectra, from 210 to 380 cm^{-1} is analyzed. This part of the spectra is shown in Fig. 6c for previously chosen set of samples. The brookite modes are located as follows: A_{1g} ($\sim$247 cm^{-1}), B_{3g} ($\sim$288 cm^{-1}), B_{1g} ($\sim$322 cm^{-1}), and B_{2g}($\sim$366 cm^{-1}) [38]. Low intensities and large widths of these modes indicate great disorder and partial amorphization of brookite in all the samples. To estimate the amount of brookite phase, the sum of the integrated intensities of Lorentzian peaks, originating from the brookite modes (ΣI_B), was compared to the intensity of Lorentzian peak related to the B_{1g} mode of anatase phase ($I_A(B_{1g})$). Although the estimation of brookite modes intensities is unreliable to some extent, due to mode overlapping, a variation in brookite content with synthesis conditions may be roughly estimated from the intensity ratio of brookite to anatase modes, $\Sigma I_B/I_A(B_{1g})$, shown in Fig. 8. In such a way, the amount of brookite phase in the samples synthesized with NH_4OH basic solution is higher than in the samples synthesized with NaOH basic solution.

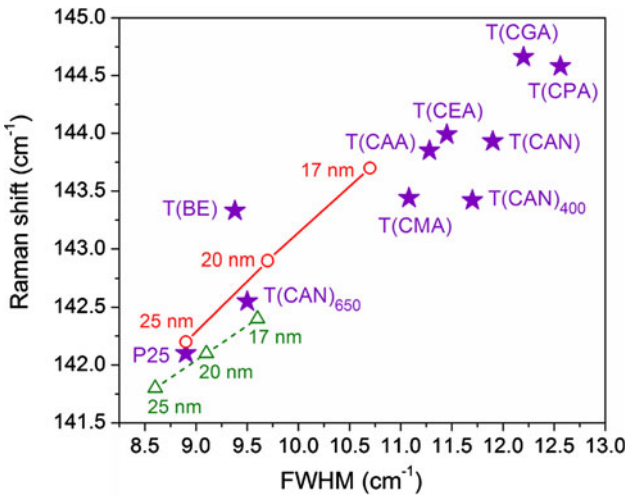

Fig. 7 The relationship between Raman shift and FWHM of E_g mode of anatase phase in TiO_2 nanopowders. The experimental values are denoted by *stars* (the calcination temperature is intentionally omitted in the names of all samples calcined at 550 °C for the clarity). *Open symbols* denote the values calculated by PCM without strain (*triangles*), and including strain effect (*circles*)

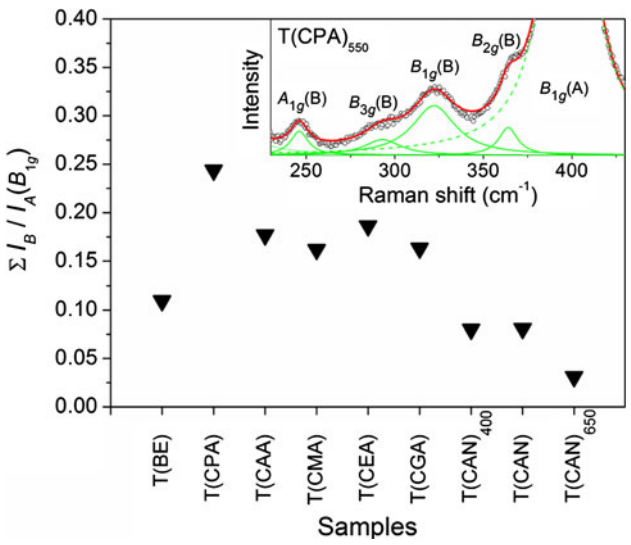

Fig. 8 The ratio of the total brookite modes intensity, ΣI_B, and the anatase B_{1g} Raman mode intensity $I_A(B_{1g})$ in TiO_2 nanopowders. The *inset*: Lorentzians of brookite modes in the experimental Raman spectra of sample $T(CPA)_{550}$. (The calcination temperature is omitted in the names of the samples calcined at 550 °C for clarity)

Note also that additional mode at about ~275 cm^{-1}, which can be related to the sodium titanate [39], is registered in the Raman spectra of the samples synthesized from NaOH basic solution.

The Raman spectra in the region from 350 to 700 cm^{-1} (Fig. 6d) of all TiO_2 nanopowders are dominated by anatase modes B_{1g} (~399 cm^{-1}), $A_{1g} + B_{1g}$ (~518 cm^{-1}), and E_g (~639 cm^{-1}) [40]. However, the modes of rutile phase, E_g (~447 cm^{-1}) and A_{1g} (~612 cm^{-1}) [40], appear in this region in the spectra of samples $T(BE)_{550}$ (synthesized with tetrabutyl titanate as a precursor) and $T(CAN)_{650}$ (calcined at 650 °C), as well as in Degussa P25.

Compared with IR spectroscopy [41], Raman spectroscopy has rarely been applied to study the surface complex formation at anatase nanoparticles [42]. Namely, in C–H and O–H spectral region, Raman features are hard to resolve as sample luminescence is often too intensive. Nevertheless, we demonstrate here the applicability of Raman spectroscopy to identify specified surface groups and estimate their amount at the surface of TiO_2 nanoparticles.

Raman spectra of representative TiO_2 nanopowders in the region between 1,000 and 4,000 cm^{-1} are shown in Fig. 9. This region is dominated by the broad feature between 2,800 and 3,800 cm^{-1} and less intensive mode at about 1,650 cm^{-1}. According to many vibrational studies, carried out to determine the characteristics of water molecules and hydroxyl groups adsorbed on anatase surfaces [29 and references therein], broad Raman structure in the

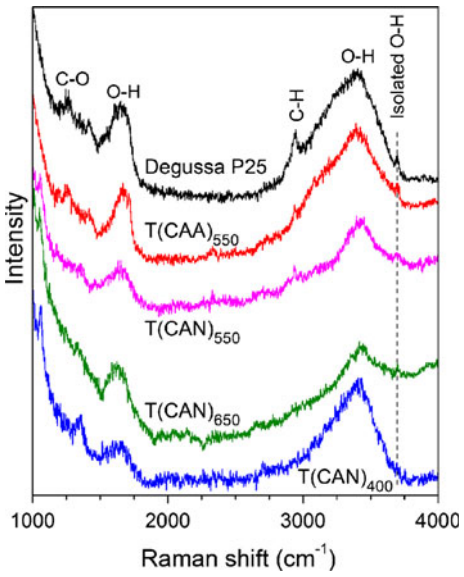

Fig. 9 The Raman spectra of TiO_2 nanopowders in the C–H and O–H spectral region (1,000–4,000 cm^{-1}). The spectra of some powders are upshifted for clarity

frequency range of 2,800–3,800 cm^{-1} can be assigned to O–H stretching vibration of water molecules adsorbed on the surface of the particles and condensed in the pores of TiO_2 nanopowders [42]. The intensity of this structure is the highest in the Raman spectra of Degussa P25 and $T(CAA)_{550}$, followed by $T(CAN)_{400}$, implying that the amount of adsorbed water molecules is the greatest in those samples. Also, the feature peaked at the frequency between 1,625 and 1,670 cm^{-1}, which can been assigned to the bending modes of adsorbed water [29], is the most intensive in Degussa P25 and $T(CAA)_{550}$. Complex shape and wideness of the spectral features described above point out to the variety of components in this range, indicating the presence of several types of surface sites bearing hydroxyl groups and adsorbed H_2O molecules [43, 44].

In addition, several sharp peaks are noticed in the Raman spectra shown in Fig. 9. A sharp peak at ~1,055 cm^{-1}, registered in the spectra of $T(CAN)_{400}$, $T(CAN)_{550}$ and $T(CAN)_{650}$, most probably belongs to stretching vibration of NO_3^-, due to the presence of $NaNO_3$ [45], as a consequence of using NaOH basic solution in the synthesis process. The peaks in the frequency range 1,200–1,500 cm^{-1}, most prominent in Degussa P25 and $T(CAA)_{550}$, can be associated with carbonate groups [23], whereas the peak at 2,940 cm^{-1} can be assigned to the stretching mode characteristic for CH- species [46].

However, low intensity peak located at ~3,700 cm^{-1} noticeable in all the samples except $T(CAN)_{400}$, is the most interesting one in our analysis. Namely, this feature, which is assigned to the O–H stretching mode of isolated (free) hydroxyls [29], can be related to the ability of the anatase samples to form the surface O–H groups with the important influence on their catalytic activity [47]. According to several authors, the hydroxyl groups with vibration frequency at about 3,700 cm^{-1} are the most photocatalytically active among all hydroxyl groups at the surface of TiO_2 nanoparticles [23].

The analysis of Raman data presented above has demonstrated the ability of Raman spectroscopy not only to characterize TiO_2 in terms of structure and crystallite size, the presence of different crystal modifications, microstrain and nonstoichiometry, but also to recognize surface O–H groups in TiO_2 nanopowders, important for photocatalytic activity.

3.6 Photocatalysis

The influence of the different synthesis parameters on the photocatalytic activity of TiO_2 nanopowders was studied on the example of the photocatalytic degradation of MET under UV light irradiation. The results are presented in Fig. 10, together with the results obtained using commercially available Degussa P25.

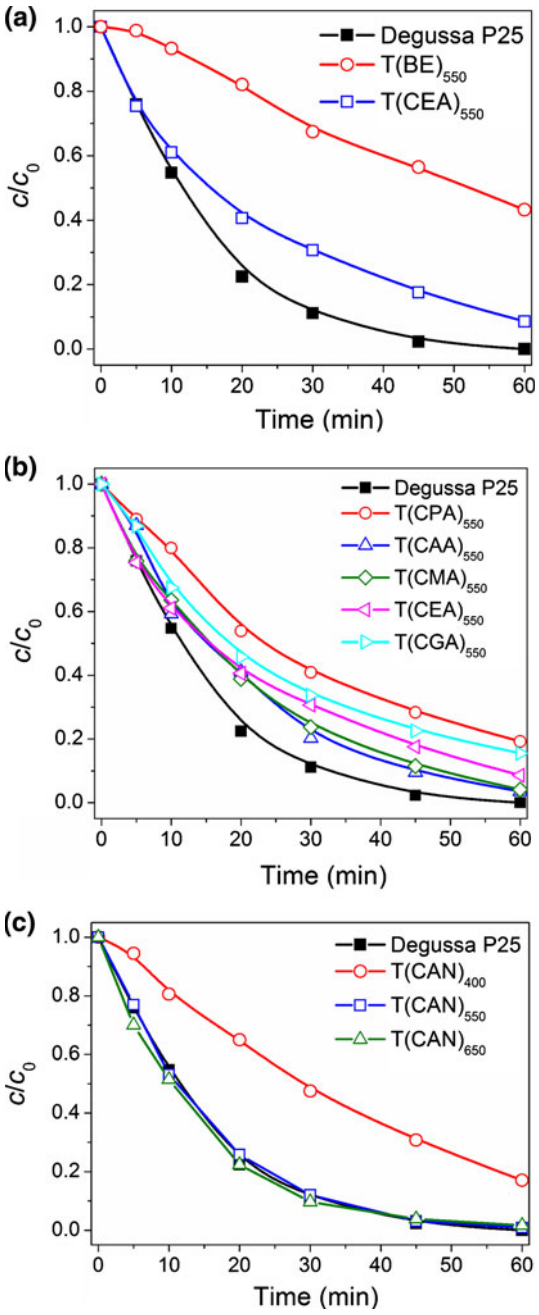

Fig. 10 Kinetics of photocatalytic degradation of MET ($c_0 = 0.05$ mM) in the presence of sol–gel synthesized TiO_2 nanopowders and Degussa P25 (1.0 mg mL^{-1}). The influence of different synthesis parameters: **a** precursor **b** alcohol and **c** calcination temperature

The Fig. 10a illustrates the influence of the type of precursor on TiO_2 nanopowders photocatalytic activity in the photodegradation of MET. As can be seen, the catalytic activity of TiO_2 nanopowders synthesized with titanium tetrachloride as the precursor is much higher, but still somewhat lower than of Degussa P25.

The influence of the type of alcogel on photocatalytic activity of TiO_2 nanopowders (Fig. 10b) was examined using different alcohols. As can be seen, the highest photocatalytic activity showed the catalysts obtained using methanol and amylalcohol.

The Fig. 10c shows the influence of calcination temperature on the photocatalytic activity of TiO_2 nanopowders on the MET photodegradation. It can be seen that the TiO_2 nanopowders calcined at ≥550 °C showed higher photocatalytic activity, even slightly higher than Degussa P25.

Since $T(CAN)_{650}$ showed the highest photocatalytic activity in the photodegradation of MET, the effect of TiO_2 loading on the efficiency of MET photodegradation was examined in the loading range from 0.5 to 5.0 mg mL^{-1} (Fig. 11a). As can be seen, with the increase of the TiO_2 loading up to 2 mg mL^{-1}, the degradation rate increases, and afterwards decreases. Theoretically, the increase in the catalyst loading above an optimum value has no effect on the photodegradation rate since all available light is already utilized. However, higher loading of TiO_2 led to the

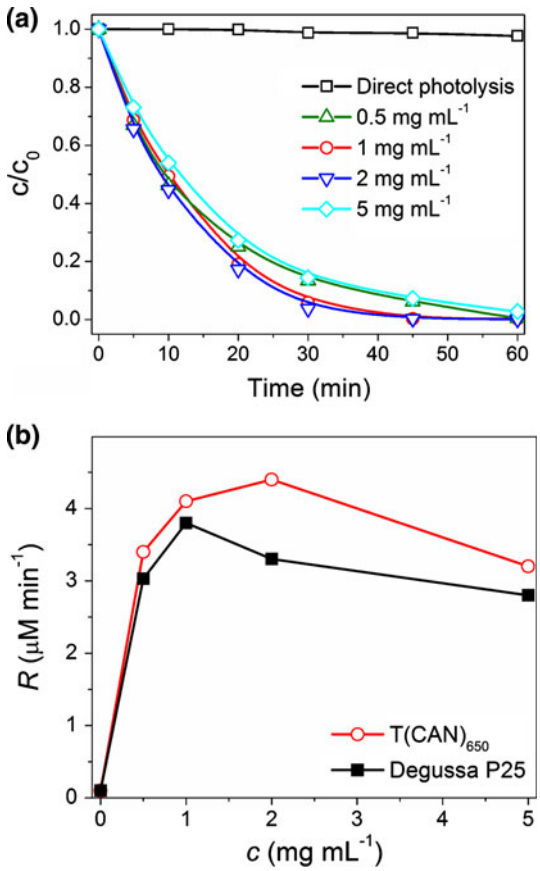

Fig. 11 **a** The effect of $T(CAN)_{650}$ loading on the kinetics of MET ($c_0 = 0.05$ mM) degradation; **b** The influence of TiO_2 loading on MET ($c_0 = 0.05$ mM) degradation rate determined for the first 20 min of irradiation

aggregation of its particles and thus to a decrease in the contact surface between the reactant and photocatalyst particles, which caused a decrease in the number of active sites, resulting in a lower rate of photodegradation. Also, when TiO_2 was overdosed, the intensity of the incident UV light was attenuated because of the decreased light penetration and increased scattering, which attenuated the positive effect coming from the dosage increment, and therefore the overall performance decreased [48].

A similar effect was also observed with Degussa P25 (Fig. 11b), but the optimal TiO_2 loading was 1 mg mL^{-1}. It should be pointed out that, $T(CAN)_{650}$ showed higher photocatalytic activity in the whole range of the catalyst loading.

4 Discussion

On the basis of experimental results presented in previous sections, we shall analyze the dependence of TiO_2 nanopowder properties on sol–gel synthesis conditions, and the impact of their structural, morphological and surface properties on photocatalytic degradation of metoprolol under UV irradiation.

Structural analysis of synthesized nanopowders, performed by XRD and Raman spectroscopy, has shown that the sample $T(CAN)_{650}$, with the majority of structural characteristics similar to Degussa P25, has the highest photocatalytic activity. Namely, the mixture of anatase and rutile (with negligible amount of brookite) in this sample is similar to Degussa P25. At the same time, high intensity of Raman signal of $T(CAN)_{650}$, with the position and linewidth of E_g anatase mode (the closest to Degussa P25 among all synthesized powders) points to high crystalline quality of anatase of this sample. However, notice that $T(BE)_{550}$ also has intensive Raman signal, with narrow E_g anatase mode, but its catalytical activity is relatively poor compared to $T(CAN)_{650}$. Despite that, $T(CAN)_{550}$ has lower Raman intensity, with considerably greater blueshift and linewidth of E_g mode, but its photocatalytic activity is close to $T(CAN)_{650}$. From this point of view we may conclude that structural properties of nanopowders have some impact on photocatalytic activity, but not crucial.

On the other side, the results obtained from BET analysis for specific surface area, and especially pore size distribution, lead to unambiguous conclusions. Namely, larger surface area and greater number of pores with dimensions in mesoporus region (>2 nm), produce higher photocalytical degradation of metoprolol, as a material with relatively large molecules (1.7 nm in length). Note that higher mesoporosity is obtained in the samples synthesized in the presence of amyl-alcohol and is getting higher with increase of calcination temperature up to 650 °C.

Special attention must be also paid to analyze the amount of surface O–H groups in TiO_2 nanopowders. Firstly, the lattice contraction, obtained by XRD analysis, points to increased hydration in all synthesized nanopowders. Also, the results for chemical composition obtained from EDS analysis, show higher oxygen content than in stoichiometric TiO_2 for majority of the samples, except the sample $T(CAN)_{550}$, which is obviously nonstoichiometric. However, the EDS results cannot give information about the form of the excess oxygen in TiO_2 (which can be in the form of interstitial oxygen in the lattice, molecular oxygen at the surface or oxygen participating in OH groups). More information on the character and amount of O–H groups in our powders we obtained from IR, and especially from Raman spectra in the C–H and O–H spectral region. These results show that the frequencies and character of surface hydroxyl modes strongly depend on the morphology of the nanoparticles, sol–gel routes and type of TiO_2 crystallites (anatase or rutile) formed during thermal treatment.

According to the presented results, the content of surface O–H groups, mostly related to adsorbed water molecules, is the highest in $T(CAA)_{550}$, followed by $T(CAN)_{400}$. However, in terms of photocatalytic activity, the presence of isolated hydroxyl groups on the surface of TiO_2 is more important than the amount of adsorbed water molecules and surface hydroxyl groups [49]. Namely, it has been recently demonstrated that surface hydroxyl groups, which can trap holes to generate the photocatalytically important active species, i.e. $^{\bullet}OH$ radicals, represent decisive factor in high photocatalytic activity of TiO_2 [49]. Reactive hydroxyl radicals $^{\bullet}OH$ are the precursors of degradation of any organic and inorganic compound and the first step in the photocatalytic degradation is the formation of the hydroxyl radicals from the TiO_2 surface [50]. Indeed, the Raman results presented in Fig. 9 show that, despite the highest intensity of Raman modes associated to O–H groups related to adsorbed water in samples $T(CAA)_{550}$ and $T(CAN)_{400}$, these samples exhibit worse photocatalytic activity than $T(CAN)_{550}$ and $T(CAN)_{650}$. Note that the presence of high water content in $T(CAN)_{400}$ is surely related to relatively low calcination temperature (400 °C). Moreover, the appearance of mode at about 3,700 cm^{-1}, originating from isolated O–H groups, in the Raman spectra of all samples with relatively high photocatalytic activity (including Degussa P25), and the absence of this mode in $T(CAN)_{400}$ with relatively poor activity, confirm the conclusions proposed above [49, 50].

5 Conclusion

We have demonstrated that highly photoactive nanocrystalline TiO_2 powders can be produced by appropriate

choice of sol–gel synthesis parameters. Different mixtures of TiO_2 crystal modifications (anatase, rutile, and brookite) are obtained with proper choice of synthesis parameters: the type of precursor, alcohol and basic solution, as well as the calcination temperature. It is noticed that the content of brookite decreases photocatalytic activity in synthesized nanopowders with other properties comparable. On the other side, the amount of rutile does not have critical impact on the photocatalytic activity. The photocatalytic performances have been attributed to the anatase particle size and crystalline quality, rather than to the presence of rutile phase. Namely, the photocatalytic activity of TiO_2 nanopowders mostly depends on anatase structure (crystallinity, particle size, microstrain, and nonstoichiometry) and porosity, as well as the amount of surface O–H groups, which can produce hydroxyl radicals. Additionally, pore size distribution in TiO_2 nanopowders has crucial role in photocatalytic degradation of metoprolol, as a material with relatively large molecules. According to this, the highest photocatalytic degradation of MET is obtained for the sample synthesized by sol–gel routine with $TiCl_4$ as a precursor, in the presence of amyl-alcohol and NaOH as basic solution, and calcined at 650 °C.

Acknowledgments This work was financially supported by the Serbian Ministry of Education and Science Projects No. III45018, ON171032, and ON172042, as well as SASA project F-134, and the Swiss National Science Foundation through Grant No. IZ73Z0-128169.

References

1. Klavarioti M, Mantzavinos D, Kassinos D (2009) Environ Int 35:402–417
2. Ikehata K, Naghashkar NJ, El-Din MG (2006) Ozone-Sci Eng 28:353–414
3. Alder AC, Schaffner C, Majewsky M, Klasmeier J, Fenner K (2010) Water Res 44:936–948
4. Rivas FJ, Gimeno O, Borralho T, Carbajo M (2010) J Hazard Mater 179:357–362
5. Liu QT, Cumming RI, Sharpe AD (2009) Photochem Photobiol Sci 8:768–777
6. Piram A, Salvador A, Verne C, Herbreteau B, Faure R (2008) Chemosphere 73:1265–1271
7. Dalrymple OK, Yeh DH, Trotz MA (2007) J Chem Technol 82:121–134
8. Yang H, An T, Li G, Song W, Cooper WJ, Luo H, Guo X (2010) J Hazard Mater 179:834–839
9. Romero V, De la Cruz N, Dantas RF, Marco P, Giménez J, Esplugas S (2011) Catal Today 161:115–120
10. Abramović B, Kler S, Šojić D, Laušević M, Radović T, Vione D (in press) J Hazard Mater
11. Doll TE, Frimmel FH (2003) Chemosphere 52:1757–1769
12. Colón G, Hidalgo MC, Navío JA (2001) J Photoch Photobiol A 138:79–85
13. Hurum DC, Agrios AG, Gray KA, Rajh T, Thurnauer MC (2003) J Phys Chem B 107:4545–4549
14. Baiju KV, Shukla S, Sandhya KS, James J, Warrier KGK (2007) J Phys Chem C 111:7612–7622
15. Golubović A, Šćepanović M, Kremenović A, Aškrabić A, Berec V, Dohčević-Mitrović Z, Popović ZV (2009) J Sol–Gel Sci Techn 49:311–319
16. Du YL, Deng Y, Zhang MS (2006) J Phys Chem Solids 67:2405–2408
17. Bala H, Guo Y, Zhao X, Zhao J, Fu W, Ding X, Jiang Y, Yu K, Lv X, Wang Y (2006) Mater Lett 60:494–498
18. Liu AR, Wang SM, Zhao YR, Zheng Z (2006) Mater Chem Phys 99:131–134
19. Sugimoto T, Zhou X, Muramatsu A (2003) J Colloid Interf Sci 259:43–52
20. Swamy V, Menzies D, Muddle BC, Kuznetsov A, Dubrovinsky LS, Dai Q, Dmitriev V (2006) Appl Phys Lett 88(1–3):243103
21. Li G, Li L, Boerio-Goates J, Woodfield BF (2005) J Am Chem Soc 127:8659–8666
22. Kraus W, Nozle G (2000) Power cell program for windows. BAM, Berlin
23. Begin-Colin S, Gadalla A, Le Caer G, Humbert O, Thomas F, Barres O, Villieras F, Toma LF, Bertrand G, Zahraa O, Gallart M, Honerlage B, Gilliot P (2009) J Phys Chem C 113:16589–16602
24. Gonzalez RJ, Zallen R, Berger H (1997) Phys Rev B 55: 7014–7017
25. Gervais F, Baumard JF (1977) Solid State Commun 21:861–865
26. Grujić-Brojčin M, Šćepanović MJ, Dohčević-Mitrović ZD, Hinić I, Matović B, Stanišić G, Popović ZV (2005) J Phys D Appl Phys 38:1415–1420
27. Franking RA, Landis EC, Hamers RJ (2009) Langmuir 25: 10676–10684
28. Li L, Shen Q, Cheng J, Hao Z (2010) Catal Today 158:361–369
29. Soria J, Sanz J, Sobrados I, Coronado JM, Maira AJ, Hernandez-Alonso MD, Fresno F (2007) J Phys Chem C 111:10590–10596
30. Goncalves RH, Schreiner WH, Leite ER (2010) Langmuir 26:11657–11662
31. Araña J, Doña-Rodrıguez JM, González-Díaz O, Tello Rendón E, Herrera Melián JA, Colón G, Navío JA, Pérez Peña J (2004) J Mol Catal A-Chem 215:153–160
32. Šćepanović MJ, Grujić-Brojčin MU, Dohčević-Mitrović ZD, Popović ZV (2006) Mat Sci Forum 518:101–106
33. Šćepanović MJ, Grujić-Brojčin MU, Dohčević-Mitrović ZD, Popović ZV (2007) Appl Phys A 86:365–371
34. Wang X, Shen J, Pan Q (2011) J Raman Spec 42:1578–1582
35. Spanier JE, Robinson RD, Zhang F, Chan S-W, Herman IP (2001) Phys Rev B 64(1–8):245407
36. Grujić-Brojčin MU, Šćepanović MJ, Dohčević-Mitrović ZD, Popović ZV (2009) Acta Phys Polonica A 116:5–54
37. Parker JC, Siegel RW (1990) Appl Phys Lett 57:943–945
38. Tompsett GA, Bowmaker GA, Cooney RP, Metson JB, Rodgers KA, Seakins JM (1995) J Raman Spectrosc 26:57–62
39. Liu H, Yang D, Zheng Z, Ke X, Waclawik E, Zhu H, Frost RL (2010) J Raman Spectrosc 41:1331–1337
40. Zhang Y-H, Chan CK, Porter JF, Guo W (1998) J Mater Res 13:2602–2609
41. Deiana C, Fois E, Coluccia S, Martra G (2010) J Phys Chem C 114:21531–21538
42. Watson S, Beydoun D, Scott J, Amal R (2004) J Nanoparticle Res 6:193–207
43. Cerrato G, Magnacca G, Mortera C, Montero J, Anderson JA (2009) J Phys Chem C 113:20401–20410
44. Martra G (2000) Appl Catal A: General 200:275–285
45. Asher SA, Tuschel DD, Vargson TA, Wang L, Geib SJ (2011) J Phys Chem A 115:4279–4287
46. Brownson JRS, Tejedor–Tejedor MI, Andersonbrownson MA (2005) Chem Mater 17:6304–6310

47. Yang D, Liu H, Zheng Z, Yuan Y, Zhao J, Waclawik ER, Ke X, Zhu H (2009) J Am Chem Soc 131:17885–17893
48. Abramović B, Šojić D, Despotović V, Vione D, Pazzi M, Csanádi J (2011) Appl Catal B Environ 105:191–198
49. Liu G, Sun C, Cheng L, Jin Y, Lu H, Wang L, Smith SC, Lu GQ, Cheng H-M (2009) J Phys Chem C 113:12317–12324
50. Vinu R, Madras G (2010) J Indian I Sci 90:189–230